Attributing the Urban–Rural Contrast of Heat Stress Simulated by a Global Model⌀

Yue Qin[⊙],[a] Weilin Liao,[b] and Dan Li[a]

[a] *Department of Earth and Environment, Boston University, Boston, Massachusetts*
[b] *Guangdong Key Laboratory for Urbanization and Geo-simulation, School of Geography and Planning, Sun Yat-sen University, Guangzhou, China*

ABSTRACT: The two-resistance mechanism (TRM) attribution method, which was designed to analyze the urban–rural contrast of temperature, is improved to study the urban–rural contrast of heat stress. The improved method can be applied to diagnosing any heat stress index that is a function of temperature and humidity. As an example, in this study we use it to analyze the summertime urban–rural contrast of simplified wet bulb globe temperature (SWBGT) simulated by the Geophysical Fluid Dynamics Laboratory land model coupled with an urban canopy model. We find that the urban–rural contrast of SWBGT is primarily caused by the lack of evapotranspiration in urban areas during the daytime and the release of heat storage during the nighttime, with the urban–rural differences in aerodynamic features playing either positive or negative roles depending on the background climate. Compared to the magnitude of the urban–rural contrast of temperature, the magnitude of the urban–rural contrast of SWBGT is damped due to the moisture deficits in urban areas. We further find that the urban–rural contrast of 2-m air temperature/SWBGT is fundamentally different from that of canopy air temperature/SWBGT. Turbulent mixing in the surface layer leads to much smaller urban–rural contrasts of 2-m air temperature/SWBGT than their canopy air counterparts.

SIGNIFICANCE STATEMENT: Heat leads to serious public health concerns, but urban and rural areas have different levels of heat stress. Our study explains the magnitude and pattern of the simulated urban–rural contrast in heat stress at the global scale and improves an attribution method to quantify which biophysical processes are mostly responsible for the simulated urban–rural contrast in heat stress. We highlight two well-known causes of higher heat stress in cities: the lack of evapotranspiration and the stronger release of heat storage. Meanwhile, we draw attention to the vegetation types in rural areas, which determine the urban–rural difference in surface roughness and significantly affect the urban–rural difference in heat stress. Last, we find the urban–rural contrasts of 2-m air temperature/SWBGT are largely reduced relative to their canopy air counterparts due to the turbulent mixing effect.

KEYWORDS: Atmosphere-land interaction; Surface fluxes; Land surface model; Heat islands; Urban meteorology

1. Introduction

Prolonged exposure to heat leads to serious health problems such as heat exhaustion, heatstroke, and heart diseases (Matthies et al. 2008). In 2003 and 2010, Europe and Russia experienced unprecedented heatwaves, causing around 40 000 and 55 000 deaths, respectively (Robine et al. 2008; Barriopedro et al. 2011). More recently in June 2021, the Pacific Northwest of the United States and Canada experienced record-breaking high temperatures far above 104°F, leading to spikes in death and sharp increases in hospital visits (World Meterological Organization 2021). Heat is now widely recognized as the number one weather killer in the United States (National Weather Service 2021).

Urban residents are often believed to experience higher heat stresses due to the higher temperatures in cities compared to the surrounding suburban and rural areas, which is known as the urban heat island (UHI) effect. Much effort has been made to understand the influence of cities on weather and climate (Howard 1833; Landsberg 1981; Oke 1978; Seto and Shepherd 2009, and references therein), especially the UHI effect (Oke 1981, 1982; Yow 2007; Grimmond 2007; McCarthy et al. 2010; Oleson 2012). Nowadays it is known that the UHI effect is caused by many factors, including the lack of vegetation, the use of man-made materials with large thermal admittance, the radiative trapping effect of the three-dimensional urban canyon, and the anthropogenic heat emissions in cities (Oke et al. 2017). Increasingly sophisticated urban parameterizations have been developed to represent urban land surface and hydrological processes in numerical weather prediction models, global climate models, and Earth system models, allowing the simulation of UHI intensities across time and space (Masson 2000; Kusaka et al. 2001; Oleson et al. 2008b,a; Grimmond et al. 2010, 2011; Oleson et al. 2011; Li et al. 2016a,b; Best and Grimmond 2015).

However, ambient temperature is not the only environmental component of heat stress (Fanger 1972). When considering human thermal comfort and heat-related health issues, it is often important to also consider humidity because evaporation of sweat is a primary method for the human body to dissipate heat (Sherwood and Huber 2010). Although the urban

---

⌀ Supplemental information related to this paper is available at the Journals Online website: https://doi.org/10.1175/JCLI-D-22-0436.s1.

Corresponding author: Yue Qin, yueqin@bu.edu

temperature is generally higher than the rural temperature, the humidity levels in cities are often lower than those in rural areas (Oke et al. 2017), offsetting some of the enhanced heat stresses induced by the UHI effects (Chakraborty et al. 2022). Other factors such as radiation and wind speed also play important roles (Fanger 1972) and a large number of heat stress indices exist in the literature with different assumptions built into them (Anderson et al. 2013; Buzan et al. 2015).

In the climate modeling literature, a primary focus of previous studies has been quantifying how heat stress changes under a warming climate (Willett and Sherwood 2012; Dunne et al. 2013; Zhang et al. 2021). Only a handful of studies specifically examined the urban–rural contrast of heat stress and how urban and rural heat stresses respond to climate change differently. Based on simulations with the Community Climate System Model whose land component, the Community Land Model (CLM), includes an urban canopy model (UCM), Fischer et al. (2012) found that the humidity deficits offset the enhanced heat stresses in urban areas due to the UHI effects, but only weakly. Moreover, they reported that the positive urban–rural contrast of heat stress is most pronounced at night and over midlatitudes and subtropics. Oleson et al. (2015) examined five heat stress indices [i.e., the National Weather Service heat index, the apparent temperature, the simplified web bulb globe temperature (SWBGT), the humidex, and the discomfort index] over North America using CLM. They highlighted that both the present-day urban–rural contrast of heat stress and the climate change impact on heat stress are highly dependent on which heat stress index is used and the urban density.

Different from previous work which largely focused on simulating the urban–rural contrast of heat stress in historical and future climates, the goal of this study is to quantify which biophysical processes (and their parameterizations) are mostly responsible for the simulated urban–rural contrast of heat stress by a global model. The premise is that only by doing so can we explain the magnitude and pattern of the simulated urban–rural contrast of heat stress by a model, as well as the differences in the simulated results by different models. To accomplish this, we develop an attribution method for the urban–rural contrast of heat stress indices that are functions of temperature and humidity, building on a recent method (Rigden and Li 2017) that has been used to attribute the urban–rural contrast of temperature (or the UHI intensity). Then we apply the improved method to analyzing the urban–rural contrast of SWBGT simulated by the Geophysical Fluid Dynamics Laboratory land model coupled with a UCM.

Here we note that recent studies reported biases associated with the SWBGT relative to the web-bulb globe temperature (WBGT) (Grundstein and Cooper 2018; Kong and Huber 2022) because the SWBGT does not consider wind and radiation factors, which vary with the vegetation density and/or land surface type (Middel et al. 2021). Nonetheless, the use of SWBGT in this study serves as an example to demonstrate how the improved method can be applied to analyzing any heat stress indices as long as they are only functions of temperature and humidity, including the National Weather Service heat index, the apparent temperature, the humidex, and so on (Anderson et al. 2013). The improved method does not apply to heat stress indices that are also functions of wind speed and radiation (e.g., the WBGT and the discomfort index), the attribution analysis of which is left for future studies.

The paper is organized as follows: Section 2 describes the model simulations and the attribution method; section 3 discusses the results; section 4 concludes the study; section 5 discusses the implications.

2. Methods

a. Model simulations

In this study, we use outputs from an offline global simulation conducted with the Geophysical Fluid Dynamics Laboratory (GFDL) land model (LM4.0), coupled with a UCM. The simulation, at a resolution of $2° \times 2.5°$, is forced by a 50-yr (1949–2000), 3-hourly, 1° dataset, which is based on a combination of observational and reanalysis data (Sheffield et al. 2006). We recycle the first 30-yr forcing to the period of 1700–1948 to spin up the model, and the simulation covers from 1949 to 2000. In this study, we focus on the summer seasons in 1981–2000, defined as June, July, and August in the Northern Hemisphere and December, January, and February in the Southern Hemisphere. We only analyze grid cells with urban fractions larger than 0.1%.

A brief description of the model structure is given here. In this modeling system, there can exist five different land-use/land-cover types (i.e., natural vegetation, secondary vegetation, grassland, pasture, and urban), which will be called tiles hereafter, in a grid cell. Among them, the nonurban tiles (i.e., natural vegetation, secondary vegetation, grassland, and pasture) are treated as rural tiles. The urban tile includes a roof component and a canyon component. The canyon component further includes the pervious ground, the impervious ground, the walls, and the vegetation inside the canyon. Detailed parameterizations of physical processes in urban areas, including those associated with urban vegetation, can be found in Li et al. (2016a). Validation of the UCM's performance at flux sites can be found in Li et al. (2016a). Large-scale validation of simulated urban and rural temperatures can be found in Liao et al. (2021). The fraction of different tiles is defined through the land cover input dataset used in phase 6 of the Coupled Model Intercomparison Project protocol. Hence, the fraction of the urban land, as well as the fractions of other land types, evolves in the simulation period (Li et al. 2016b).

Both LM4.0 and UCM can be viewed as multi-source models (Bonan 2019) in the sense that the vegetation and the soil ground for the rural land (or the building and the canyon floor for the urban land) have their own energy budgets and surface temperatures (e.g., T_{soil}, T_{veg}, T_{building}, T_{ground} in Fig. 1a). Note that Fig. 1 is a simplified schematic and is not to scale. The urban canyon, for example, is more complicated and is composed of four facets (the walls, the impervious surface at the ground, the pervious ground, and the vegetation above the pervious ground). The connection between these different
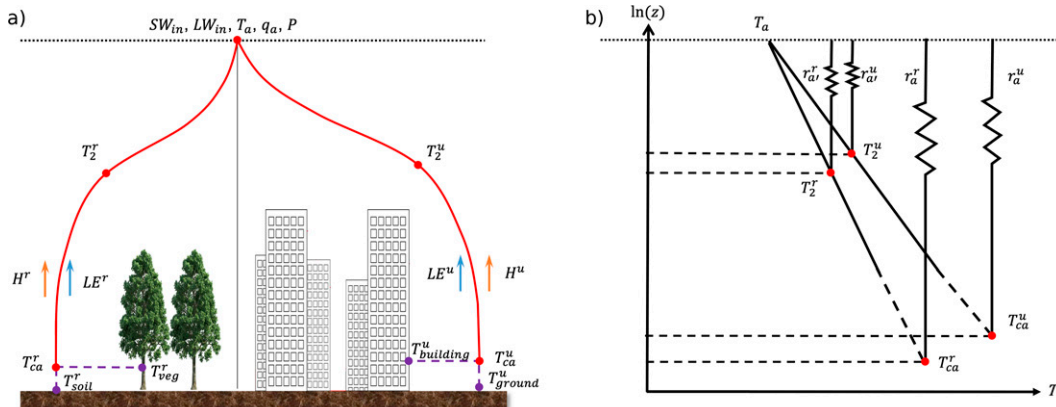
FIG. 1. (a) A schematic of the temperature and humidity definitions. The superscripts u and r represent urban and rural tiles, respectively. Subscripts ca and 2 represent canopy air and 2 m above the displacement height, respectively. SW_{in}, LW_{in}, T_a, q_a, and P refer to the incoming shortwave radiation, incoming longwave radiation, the air temperature at the bottom of the atmospheric model, the specific humidity at the bottom of the atmospheric model, and the pressure, respectively. These quantities are identical for urban and rural tiles. However, urban and rural tiles have different sensible (H) and latent heat (LE) fluxes, different canopy air/2-m air temperatures as well as humidities, and different surface temperatures. (b) A schematic of how the 2-m air temperature is interpolated between the canopy air temperature and the air temperature at the bottom of the atmospheric model. Since the displacement heights and roughness lengths are different between urban and rural tiles, the canopy air and 2-m air temperature and humidity are not necessarily defined as the same physical height for urban and rural tiles. r_a refers to the bulk aerodynamic resistance to convective heat transfer between the canopy air and the bottom of the atmospheric model, while r_a' refers to the aerodynamic resistance to convective heat transfer between the 2-m level and the bottom of the atmospheric model. Although logarithmic temperature profiles are shown here for schematic purposes, the temperature profiles, in reality, are not always logarithmic due to thermal stratification.

surface temperatures is the so-called canopy air temperature (T_{ca}), where the sensible and latent heat fluxes from different facets are aggregated and passed to the atmospheric model (see Fig. 1a). The canopy air temperature is different from the air temperature (denoted as T_a) at the bottom of the atmospheric model, the height of which is usually on the order of 20–50 m. The canopy air temperature is also different from the so-called 2-m air temperature (T_2), which is computed by interpolating the surface-layer temperature profile to 2 m above the displacement height (z_d). The z_d can be regarded as the level at which the mean drag on the surface appears to act (Jackson 1981), which is close to zero if there is no canopy (vegetation or urban). The value of z_d can be on the order of 10 m for tall canopies (Garratt 1994, Table A6 therein).

Like most other land surface models, the model used here assumes that within the same grid cell, urban and rural tiles share the same atmospheric conditions (see Fig. 1a). Hence atmospheric variables (SW_{in}, LW_{in}, T_a, q_a, and P) will not contribute to urban–rural differences when urban and rural tiles are in the same grid cell. This assumption breaks down when comparing urban and rural conditions in different grid cells (e.g., in high-resolution simulations) but works for our analyses, which focus on urban–rural differences in the same grid cell. Recall that the spatial resolution of our simulation is $2° \times 2.5°$. When comparing urban and rural conditions in different grid cells, this assumption can be relaxed [see an example in Wang and Li (2021)]. To summarize, T_{ca} and T_2 are different between urban and rural tiles within the same grid cell while T_a is identical (Fig. 1).

Similarly, we define the specific humidity at the bottom of the atmospheric model (q_a), the canopy air specific humidity (q_{ca}), and also the 2-m specific humidity (q_2). We further define heat stress indices based on these temperatures and humidities. In this study, we use the SWBGT (W) (Willett and Sherwood 2012; Fischer et al. 2012; Oleson et al. 2015), which is a unitless heat stress index calculated from ambient air temperature T (K) and water vapor pressure e (Pa) as

$$W = 0.567(T - 273.15) + 0.003\,93e + 3.94. \quad (1)$$

Since the water vapor pressure is related to specific humidity q (kg kg^{-1}) and air pressure P (Pa) through $q = 0.622e/P$, the above equation can be also written as

$$W = 0.567(T - 273.15) + 0.006\,32Pq + 3.94. \quad (2)$$

Therefore, due to the different temperatures/humidities defined earlier (see Fig. 1), we have three different SWBGTs: one at the bottom of the atmospheric model (W_a), which is the same between urban and rural tiles; one in the canopy air (W_{ca}), which represents the ambient heat stress within the canopy; one at 2 m above the displacement height (W_2), which lies in between the canopy and the lowest level of the atmospheric model. Hereafter we refer to 2 m above the displacement height as the 2-m level for simplicity.

In this study, we are interested in understanding the differences between urban and rural tiles in terms of their temperatures and SWBGTs. Since the urban and rural tiles share the same atmospheric conditions, the urban–rural contrasts of

canopy air and 2-m air temperature and SWBGT must be caused by the urban–rural differences in surface biophysical properties such as albedo, roughness length, heat capacity, etc. However, these biophysical factors make unequal contributions to the urban–rural contrasts of canopy air and 2-m air temperature and SWBGT. Quantifying the contribution of each factor requires an attribution method.

b. The attribution method

1) THE TRM METHOD

The essence of the two-resistance mechanism (TRM) method (Rigden and Li 2017) is to derive an analytical solution for the surface temperature T_s (K) based on the energy balance equation for a bulk surface, from which the sensitivity of T_s to various biophysical factors can be directly computed. The connection between the bulk surface temperature defined in the TRM method and the canopy air and 2-m air temperature discussed above will be elaborated on later.

Let us start with the energy balance equation for an infinitely thin surface layer that is horizontally homogeneous:

$$R_n = \mathrm{SW_{in}}(1 - \alpha) + \varepsilon \mathrm{LW_{in}} - \varepsilon \sigma T_s^4 = H + \mathrm{LE} + G, \quad (3)$$

where R_n (W m^{-2}) is the net radiation, $\mathrm{SW_{in}}$ (W m^{-2}) is the incoming shortwave radiation, $\mathrm{LW_{in}}$ (W m^{-2}) is the incoming longwave radiation, α is the surface albedo, ε is the surface emissivity, σ (W m^{-2} K^{-4}) is the Stefan–Boltzmann constant, H (W m^{-2}) is the sensible heat flux, LE (W m^{-2}) is the latent heat flux, and G (W m^{-2}) is the ground heat flux or heat storage. The H and LE terms are further parameterized by the resistance concepts (Monteith and Unsworth 2008):

$$H = \frac{\rho c_p}{r_a}(T_s - T_a), \quad (4)$$

$$\mathrm{LE} = \frac{\rho L_v}{r_a + r_s}[q^*(T_s) - q_a], \quad (5)$$

where ρ (kg m^{-3}) is the air density, c_p (J kg^{-1} K^{-1}) is the specific heat of air at constant pressure, L_v (J kg^{-1}) is the latent heat of vaporization, $q^*(T_s)$ is the saturated specific humidity at T_s following $q^*(T_s) = 0.622 e^*(T_s)/P$, where $e^*(T_s)$ (Pa) is the saturation vapor pressure that can be computed from T_s using the Clausius–Clapeyron relation. The term r_a (s m^{-1}) is the aerodynamic resistance, which represents the efficiency of convective heat transfer between the surface and the atmosphere and is related to wind speed, roughness length, and stability conditions (Garratt 1994). The smaller the r_a is, the more efficient convective heat transfer becomes. The term r_s (s m^{-1}) is the surface resistance representing how far the surface is away from saturation, which is dependent on the water availability and vegetation characteristics (Garratt 1994). The smaller the r_s is, the closer the surface is to saturation.

Substituting Eqs. (4) and (5) into Eq. (3) and linearizing the emitted longwave radiation term and the saturated specific humidity term (Rigden and Li 2017) yields

$$T_s - T_a = \frac{\lambda_0 \left\{ R_n^* - G - \dfrac{\rho L_v}{r_a + r_s}[q^*(T_a) - q_a] \right\}}{1 + f_{\mathrm{TRM}}}, \quad (6)$$

where $R_n^* = \mathrm{SW_{in}}(1 - \alpha) + \varepsilon \mathrm{LW_{in}} - \varepsilon \sigma T_a^4$, $f_{\mathrm{TRM}} = (r_0/r_a)\{1 + (\delta/\gamma)[r_a/(r_a + r_s)]\}$, $\delta = de^*/dT|_{T_a}$, $r_0 = \rho c_p \lambda_0$, $\gamma = c_p P/(0.622 L_v)$, and $\lambda_0 = 1/(4\varepsilon \sigma T_a^3)$.

With Eq. (6), one could study the change in surface temperature (T_s) due to changes in any forcing or parameter (Liao et al. 2018; Wang et al. 2019, 2020b; Moon et al. 2020). As alluded to earlier, we are interested in using Eq. (6) to diagnose the differences between urban and rural tiles within the same grid cell simulated by the numerical model. In this case, there are no urban–rural differences in terms of $\mathrm{SW_{in}}$, $\mathrm{LW_{in}}$, T_a, q_a, and P. We also neglect the urban–rural difference in emissivity due to its small role as demonstrated elsewhere (Liao et al. 2018; Wang et al. 2020b). Therefore, we attribute the urban–rural difference in surface temperature (ΔT_s) to urban–rural differences in the albedo, aerodynamic resistance, surface resistance, and ground heat flux via the first-order Taylor expansion, as follows:

$$\Delta T_s = \frac{\partial T_s}{\partial \alpha} \Delta \alpha + \frac{\partial T_s}{\partial r_a} \Delta r_a + \frac{\partial T_s}{\partial r_s} \Delta r_s + \frac{\partial T_s}{\partial G} \Delta G. \quad (7)$$

Full expressions of the partial derivatives (called the sensitivities hereafter) can be found in the supplemental material. The product of the sensitivity and the difference $[(\partial T_s/\partial X)\Delta X]$ is denoted as the contribution of the variable X to ΔT_s.

2) EXTENDING THE TRM METHOD TO HEAT STRESS

In this section, we extend the original TRM method, which was designed to study the urban–rural contrast of temperature, to study the urban–rural contrast of heat stress. For a bulk surface, the latent heat flux can also be parameterized by the difference between the surface specific humidity q_s and the atmospheric specific humidity q_a as

$$\mathrm{LE} = \frac{\rho L_v}{r_a}(q_s - q_a). \quad (8)$$

Here r_s does not show up in the denominator because the actual specific humidity at the surface (q_s), instead of the saturated surface specific humidity, is used. Comparing Eq. (8) to Eq. (5) gives

$$q_s = \frac{r_a}{r_a + r_s}[q^*(T_s) - q_a] + q_a. \quad (9)$$

Analogous to the attribution of urban–rural difference in surface temperature, the urban–rural difference in the surface specific humidity can be expressed as

$$\Delta q_s = \frac{\partial q_s}{\partial \alpha} \Delta \alpha + \frac{\partial q_s}{\partial r_a} \Delta r_a + \frac{\partial q_s}{\partial r_s} \Delta r_s + \frac{\partial q_s}{\partial G} \Delta G. \quad (10)$$

Furthermore, based on Eq. (2), the urban–rural difference in surface SWBGT can be expressed as

$$\Delta \mathrm{W}_s = 0.567\Delta T_s + 0.00632P\Delta q_s, \quad (11)$$

where ΔT_s and Δq_s are from Eqs. (7) and (10), respectively. Namely, the contribution of the generic variable X to ΔW_s can be expressed as $[0.567(\partial T_s/\partial X) + 0.006\,32P(\partial q_s/\partial X)]\Delta X$.

As mentioned earlier, although this study only analyzes the SWBGT, the methodology can be applied to other heat stress indices (e.g., the National Weather Service heat index, the apparent temperature, the humidex). Some of these indices are functions of relative humidity and/or dewpoint temperature, but since relative humidity and dewpoint temperature are functions of temperature and specific humidity (with given pressure), they pose no additional challenge for this method. In general, if a heat stress index (HS) can be expressed as $HS = f(T, q)$, where f is a known function, its change can thus be linked to changes in T and q through $\Delta HS = (\partial f/\partial T)\Delta T + (\partial f/\partial q)\Delta q$. Furthermore, the attribution method can be further improved to study mixed effects between temperature and humidity by using a second-order (or higher-order) Taylor expansion (see Chen et al. 2020) through

$$\Delta HS = \frac{\partial f}{\partial T}\Delta T + \frac{\partial f}{\partial q}\Delta q + \frac{1}{2}\left[\frac{\partial^2 f}{\partial T^2}(\Delta T)^2 + \frac{\partial^2 f}{\partial q^2}(\Delta q)^2 \right.$$
$$\left. + 2\frac{\partial^2 f}{\partial T \partial q}\Delta T\Delta q\right].$$

In the present study, we only focus on the first-order Taylor expansion while neglecting the second- and higher-order terms and the mixed effects because these terms are usually of smaller magnitude relative to the first-order terms. However, they can be important when the assumptions underlying Taylor expansion start to break down (e.g., when the urban–rural differences of biophysical factors are no longer sufficiently small) or when one is specifically interested in the coupling and interaction of the biophysical factors.

3) APPLICATION OF THE ATTRIBUTION METHOD TO DIAGNOSING THE NUMERICAL MODEL OUTPUTS

We need to address the following three questions before applying the attribution method discussed above to diagnosing the numerical model outputs. First, which temperature and SWBGT in the numerical model represent the bulk surface temperature (T_s) and the bulk surface SWBGT (W_s) in the attribution method, respectively? Second, at which time scale should the attribution analysis be conducted? Third, how to ensure that the attribution method reasonably captures the simulated urban–rural differences in T_s and W_s by the numerical model? In this section, we address these three questions.

There is no single correct answer to the question of which temperature in the numerical model represents (or approximates) the bulk surface temperature (T_s) in the attribution method. In our opinion, the best approximation for this particular numerical model is the canopy air temperature. There are two reasons supporting this argument (with more details presented in the supplemental material). First, the total surface sensible heat flux is usually computed based on the difference between the canopy air temperature and the air temperature at the bottom of the atmospheric model in numerical models such as the LM4.0 and UCM used here. Therefore, from the atmospheric model's perspective, the canopy air temperature is the temperature at which the total surface sensible heat flux is generated (or at which the different heat sources on the land are aggregated). In other words, the canopy air temperature would be identical to the surface temperature for a bulk surface with the same total sensible heat flux and thermal roughness length (Garratt 1994). Second, the canopy air temperature agrees reasonably well with the radiative surface temperature inferred from the simulated outgoing longwave radiation via the Stefan–Boltzmann law (see Fig. S1 in the supplemental material). This is consistent with the findings in Li and Bou-Zeid (2014).

To proceed, we will use the canopy air temperature (T_{ca}) to approximate T_s in the TRM attribution method. Similarly, we also use the canopy air humidity (q_{ca}) to represent q_s and use the extended TRM attribution method [Eq. (11)] for analyzing the canopy air SWBGT. The other variables needed for the attribution can then be derived. For example, the aerodynamic resistance and the surface resistance are inferred using Eqs. (4) and (5), given the simulated T_{ca}, H, and LE, and the forcing variables T_a and q_a. The albedo is inferred using the outgoing and incoming shortwave radiation, and the ground heat flux is a default output. Note that sometimes the inferred r_a is negative when applying the TRM method (or other similar methods such as the intrinsic biophysical mechanism; see Chen and Dirmeyer 2016) to diagnosing numerical model outputs because numerical models are often dual- or multisource models while these attribution methods are designed for a bulk surface. The negative r_a (and also r_s) are removed from our analysis, following previous work (Liao et al. 2018; Wang et al. 2020b; Wang and Li 2021).

In terms of time scales, the default outputs are 3-hourly, consistent with the temporal resolution of the forcing. They are first separated into daytime and nighttime data. For simplicity, we assume that daytime is when the incoming shortwave radiation is greater than 25 W m^{-2} and nighttime is when it is less than 25 W m^{-2}. We then average the 3-hourly data to monthly daytime/nighttime data and perform the attribution at the monthly scale, following Liao et al. (2020). The attribution results are further averaged across 20 summers (1981–2000).

To ensure that the attribution method captures the simulated urban–rural differences in temperature and SWBGT by the numerical model, the sensitivities [partial derivatives in, e.g., Eq. (7)] are weighted averages of both urban and rural sensitivities. The weights are calibrated to best match the urban–rural differences calculated from the TRM method with those simulated by the numerical model, that is, by minimizing the root-mean-square error, following Liao et al. (2018).

4) FROM CANOPY AIR TEMPERATURE/SWBGT TO 2-M AIR TEMPERATURE/SWBGT

The TRM method discussed above is used to diagnose urban–rural contrasts of canopy air temperature/SWBGT. However, it is common to use the 2-m air temperature and
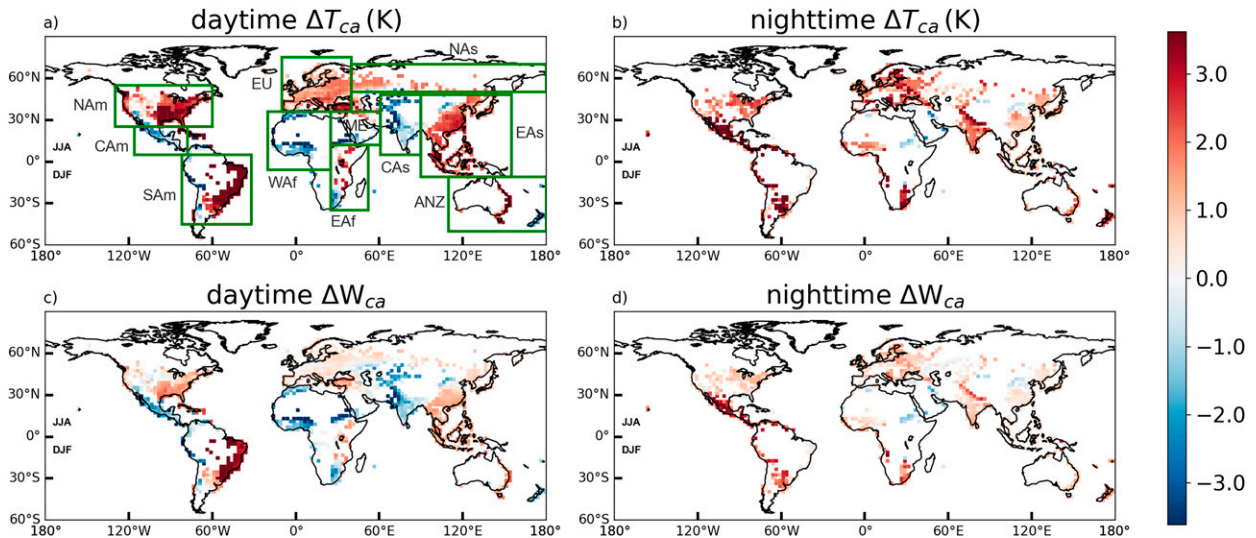
FIG. 2. Simulated urban–rural contrasts (Δ = urban − rural) of (a) daytime canopy air temperature (T_{ca}), (b) nighttime canopy air temperature, (c) daytime canopy air SWBGT (W_{ca}), and (d) nighttime canopy air SWBGT. The green boxes in (a) define the boundary of 11 regions: North America (NAm), Central America (CAm), South America (SAm), Europe (EU), Western Africa (WAf), Eastern Africa (WAf), Middle East (ME), North Asia (NAs), Central Asia (CAs), Eastern Asia (EAs), Australia/New Zealand (ANZ).

SWBGT to quantify the near-surface microclimatic conditions in the literature, even though the interpretation of "2-m" height can be ambiguous over tall canopies. Here we extend the TRM method to diagnosing urban–rural contrasts of 2-m air temperature and SWBGT. The computation and physical interpretation of the 2-m air temperature and SWBGT are detailed in the supplemental material.

Based on the concept of constant-flux layer, Wang and Li (2021) derived an expression for the 2-m air temperature T_2, as follows:

$$T_2 = \frac{r'_a}{r_a}(T_{ca} - T_a) + T_a, \qquad (12)$$

where r'_a is the aerodynamic resistance to convective heat transfer between the 2-m level and the atmosphere (see Fig. 1b). With this expression, the sensitivities of T_2 to various biophysical factors can be computed. Similarly, one can derive the sensitivities of 2-m specific humidity using the bulk parameterization for latent heat flux, and thus the 2-m SWBGT (detailed in the supplemental material).

3. Results

Figures 2 and 3 show the simulated urban–rural differences of canopy air temperature (ΔT_{ca}; Figs. 2a,b), canopy air SWBGT
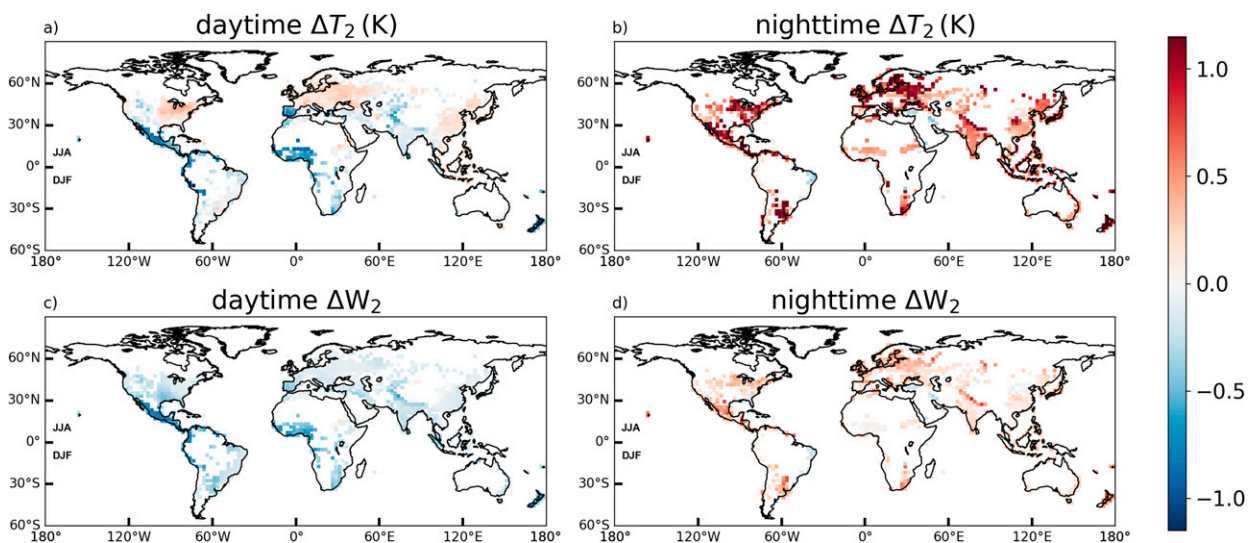

FIG. 3. Simulated urban–rural contrasts (Δ = urban − rural) of (a) daytime 2-m air temperature (T_2), (b) nighttime 2-m air temperature, (c) daytime 2-m SWBGT (W_2) and (d) nighttime 2-m SWBGT.

(ΔW_{ca}, Figs. 2c,d), 2-m air temperature (ΔT_2, Figs. 3a,b), and 2-m SWBGT (ΔW_2, Figs. 3c,d) during the daytime and nighttime, respectively. It is evident that the simulated urban–rural contrasts show large differences between daytime and nighttime, as well as strong spatial variabilities. We will first focus on understanding the general patterns in the daytime and nighttime results (sections 3a–3c), and then discuss the spatial variability (section 3d).

For ΔT_{ca} and ΔW_{ca}, the most striking feature is that some regions exhibit negative values in the daytime, such as Central America, West Africa, and Central Asia. The negative daytime ΔT_{ca} and ΔW_{ca} in these regions will be discussed in detail later. At night, ΔT_{ca} and ΔW_{ca} are mostly positive. By comparing the results for ΔT_{ca} and ΔW_{ca}, one can see that ΔW_{ca} is smaller than ΔT_{ca}, especially in areas with positive values of both. This is due to the humidity deficits in urban areas, namely, urban areas are generally hotter but drier, as alluded to earlier. Hence the enhanced heat stresses in the urban areas by the positive UHI effects are partially offset by the humidity deficits.

Comparing Figs. 3a and 3b to Figs. 2a and 2b reveals that ΔT_2 has similar spatial patterns as ΔT_{ca} but with much smaller magnitude and with more negative values during the daytime. The smaller magnitude of ΔT_2 than ΔT_{ca} is due to the role of turbulent mixing. In the surface layer (between the land model and the lowest level of the atmospheric model), turbulent eddies transport mass, momentum, and heat from the surface to the atmosphere or vice versa (Stull 1988). The turbulent transport is responsible for the logarithmic profiles under neutral conditions (or the profiles described by Monin–Obukhov similarity theory under thermally stratified conditions) in the surface layer, as illustrated in Fig. 1b. Although urban land has biophysical properties that are different from those of rural land and thus the surface conditions differ between the urban and rural land, such differences become smaller as the urban and rural fluxes become mixed and eventually disappear when the fluxes reach the lowest level of the atmospheric model.

With the turbulent mixing effects and the humidity deficits in urban areas, the daytime ΔW_2 (Fig. 3c) turns negative worldwide. Although the nighttime ΔW_2 (Fig. 3d) remains positive, the mixing effects cause its magnitude to be smaller than ΔW_{ca}.

We should highlight that ΔT_2 and ΔW_2 are not necessarily fair indicators of near-surface air temperature and heat stress differences between urban and rural areas, because T_2 and W_2 are defined at 2 m above the displacement height and the urban displacement height is often much larger than the rural counterpart except for forests (Oke et al. 2017). As a result, the height at which the 2-m air temperature is defined is usually different between urban and rural areas. We did not correct the definition of the 2-m level to be consistent with the literature, but we note that some models try to correct such effects by computing new temperature/humidity variables at 2 m above the ground (Meili et al. 2020) and other models such as CLM have the 2-m air temperature defined differently for urban and rural areas. In CLM (Oleson et al. 2013), T_{ca} is assigned to the 2-m air temperature directly for urban areas

while for rural areas the 2-m air temperature is defined at 2 m above the displacement height and interpolated between T_{ca} and T_a. This partly explains why our results of ΔT_2 are different from those from CLM (Oleson et al. 2011).

Perhaps what is more meaningful is the comparison between the daytime and nighttime results. For T_{ca} and W_{ca}, the urban–rural contrasts are stronger during the daytime; while for T_2 and W_2, the urban–rural contrasts are stronger during the nighttime. This is consistent with previous work showing that the surface UHI is often stronger during the daytime, while the near-surface UHI tends to be stronger at night (Oke et al. 2017; Stewart et al. 2021; Venter et al. 2021).

It is important to stress that the aim of this study is not to validate the results shown in Figs. 2 and 3. Instead, the goal is to quantify the contributions of different biophysical factors to the simulated ΔT_{ca}, ΔW_{ca}, ΔT_2, and ΔW_2 using the improved TRM attribution method. In the following, we first present the sensitivities of T_{ca}, W_{ca}, T_2, and W_2 to biophysical factors, followed by the urban–rural differences in biophysical factors. The products of the sensitivities and the urban–rural differences, which represent the contributions of different biophysical factors, are then presented. Last, the regionally averaged attributions are shown to highlight the spatial variability.

a. Sensitivities to biophysical factors

1) SENSITIVITIES OF HEAT STRESS AT THE CANOPY AIR LEVEL

As the first step, we calculate the sensitivities of canopy air temperature (T_{ca}) and canopy air SWBGT (W_{ca}) to biophysical factors (namely albedo, aerodynamic resistance, surface resistance, and heat storage) based on the formulas presented in the supplemental material. Because the results of T_{ca} and W_{ca} are similar in terms of the global patterns, we only present the results for W_{ca} here (Fig. 4) while the sensitivities of T_{ca} to biophysical factors can be found in the supplemental material (see Fig. S2).

First, the sensitivity of W_{ca} to albedo is negative worldwide during the daytime and is close to zero at night, as shown in Figs. 4a,b. Intuitively, the larger the surface albedo, the more solar radiation is reflected and the lower the T_{ca}, as well as the W_{ca}, which explains the negative sensitivity in the daytime. Figures 4c and 4d present the sensitivity of canopy air heat stress to aerodynamic resistance ($\partial W_{ca}/\partial r_a$). It is clear that $\partial W_{ca}/\partial r_a$ is positive worldwide during the day, but much smaller at night. As discussed in Liao et al. (2020), the positive sensitivity during the daytime implies that when the land surface becomes less efficient in transferring sensible heat to the lower atmosphere (i.e., when r_a increases), W_{ca} tends to increase. Figure 4e shows a positive signal of $\partial W_{ca}/\partial r_s$ globally during the daytime, indicating that W_{ca} increases as the land surface becomes less efficient in using energy for evapotranspiration (i.e., when r_s increases). This effect is understandably small during the nighttime (see Fig. 4f). Last, Figs. 4g and 4h show the sensitivity of W_{ca} to heat storage ($\partial W_{ca}/\partial G$) during the daytime and nighttime, respectively. Note that the ground heat flux is defined to be positive downward and negative
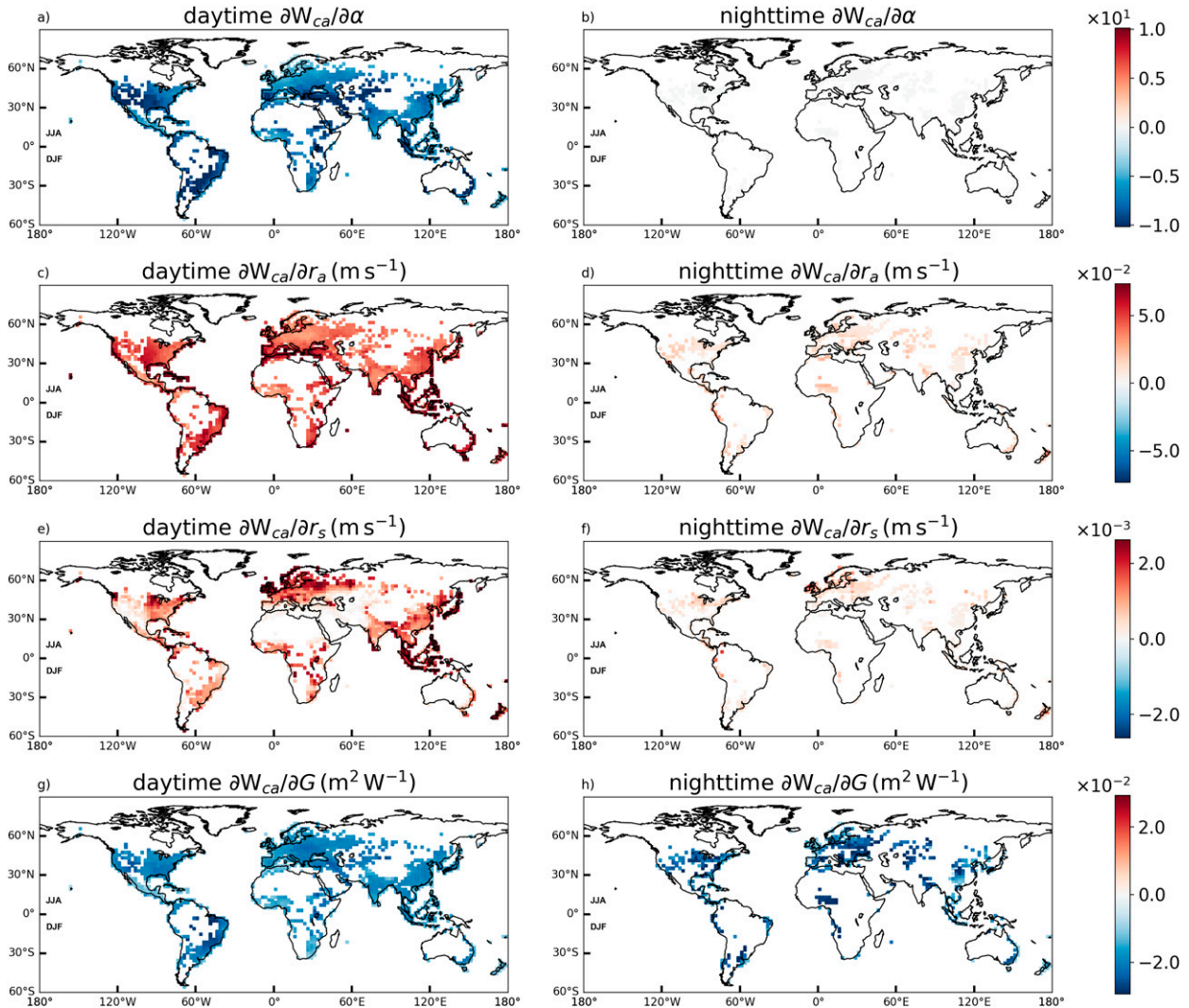
FIG. 4. The sensitivities of canopy air SWBGT to (a),(b) albedo ($\partial W_{ca}/\partial \alpha$), (c),(d) aerodynamic resistance ($\partial W_{ca}/\partial r_a$), (e),(f) surface resistance ($\partial W_{ca}/\partial r_s$), and (g),(h) heat storage ($\partial W_{ca}/\partial G$) during (left) daytime and (right) nighttime.

upward. Therefore, the fact that more ground heat flux goes downward to deeper soil layers (or built materials) during the daytime means a decrease in canopy air temperature and heat stress, leading to negative daytime $\partial W_{ca}/\partial G$. Conversely, the fact that more ground heat flux goes upward to the surface during the night means an increase in canopy air temperature and heat stress, also leading to negative nighttime $\partial W_{ca}/\partial G$. Although $\partial W_{ca}/\partial G$ is negative for both daytime and nighttime, the magnitude of $\partial W_{ca}/\partial G$ at night is larger than that in the day, showing a stronger effect of heat release on canopy air temperature and heat stress at night than during the day.

2) SENSITIVITIES OF HEAT STRESS AT THE 2-M LEVEL

Similarly, we examine the sensitivity of W_2 to albedo, surface resistance, and heat storage (see Fig. S3). Compared to the results for W_{ca}, the sensitivities of W_2 to albedo, surface resistance, and heat storage show very similar patterns but have a smaller magnitude, because these sensitivities are simply their counterparts for W_{ca} multiplied by the factor r'_a/r_a, which is smaller than unity [see Eqs. (S17)–(S20)].

The more complicated sensitivities are those to r_a (i.e., aerodynamic resistance between the surface and the atmosphere) and r'_a (i.e., aerodynamic resistance between the 2-m level and the atmosphere). Figure 5a shows that during the daytime, the sensitivity of W_2 to aerodynamic resistance ($\partial W_2/\partial r_a$) is negative. This is contrary to the positive $\partial W_{ca}/\partial r_a$ (see Fig. 4c). That is because when it is less efficient in transferring heat from the surface (or more precisely the height at which the canopy air temperature is defined) to the atmosphere (i.e., r_a increases), the air temperature and heat stress in the canopy increase while the air temperature and heat stress at the 2-m level decrease. However, if it is less efficient in transferring
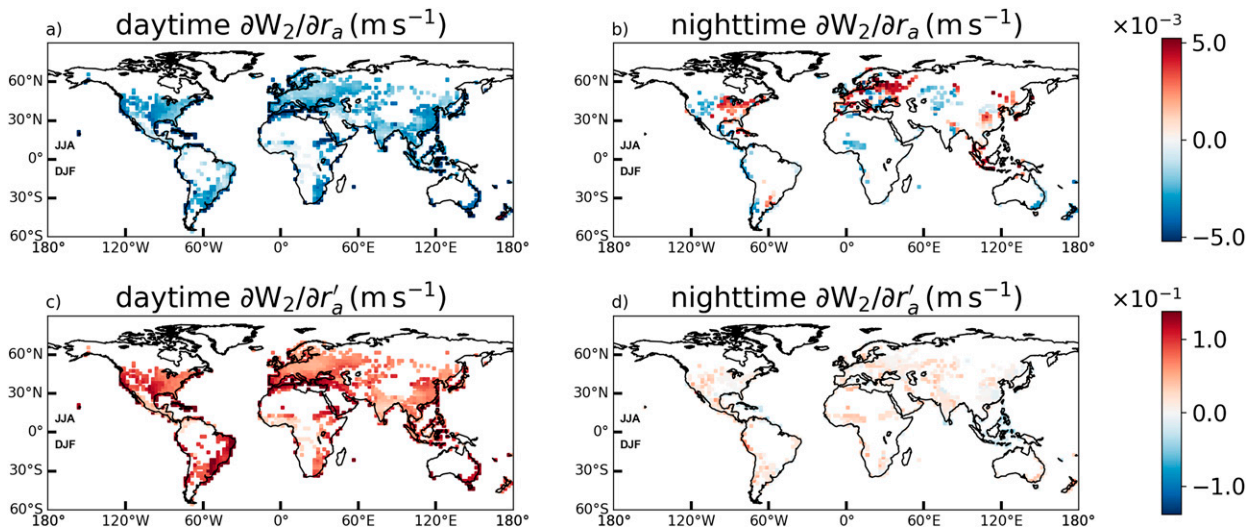
FIG. 5. The sensitivities of 2-m SWBGT to (a),(b) aerodynamic resistance ($\partial W_2/\partial r_a$), and (c),(d) 2-m aerodynamic resistance ($\partial W_2/\partial r_a'$) during (left) daytime and (right) nighttime.

heat from the 2-m level to the atmosphere (i.e., r_a' increases), the 2-m air temperature and heat stress increase, which explains the positive $\partial W_2/\partial r_a'$ during the daytime (Fig. 5c). It should be also pointed out that $\partial W_2/\partial r_a'$ is of larger magnitude than $\partial W_2/\partial r_a$, indicating that W_2 is more affected by changes in r_a' than in r_a. During the nighttime, $\partial W_2/\partial r_a$ is very heterogeneous at the global scale and $\partial W_2/\partial r_a'$ is weakly positive (Figs. 5b,d).

b. Urban–rural differences in biophysical factors

We further compare the urban–rural differences in five biophysical factors. Figures 6a and 6b show a negative contrast in albedo over most regions except for the western edge of South America, equatorial Africa, the Mediterranean region, and West Asia. The negative albedo differences imply that the urban land is parameterized with a smaller albedo than the rural land in the numerical model, while the positive albedo differences indicate the opposite. Although the radiative trapping effect tends to reduce the albedo of urban land, urban land does not always have a smaller albedo than rural land, and the urban–rural albedo differences depend on the characteristics of urban and rural land (e.g., urban form, rural vegetation type) (Oke et al. 2017). Our results here also reflect this.

The daytime contrast of aerodynamic resistance (r_a) shows strong spatial variability, which is highly related to the rural vegetation type. For example, in arid regions (i.e., Central America, Middle East, and Central Asia), rural land is characterized by vegetation of low height such as shrubs, sage brushes, and grasses, which makes it less efficient for rural land to transfer sensible heat to the atmosphere than urban land. Therefore, the urban–rural contrast in aerodynamic resistance (Δr_a) in drier regions tends to be negative, as opposed to more humid regions where rural land has taller vegetation and thus might have smaller r_a than adjacent urban land (i.e., positive in Fig. 6c). At night, Δr_a shows a negative signal

almost everywhere (Fig. 6d), particularly in densely populated regions (e.g., eastern North America, eastern South America, Europe, East Asia, and Southeast Asia), indicating that cities are more efficient in transferring heat from the surface to the lower atmosphere at night. This is consistent with the stronger release of ground heat storage in urban areas, creating more unstable stratification in the urban surface layer. In contrast, convective heat transfer is less efficient with the existence of a stable surface layer in rural areas. Previous field studies have confirmed a near-neutral or slightly unstable boundary layer in cities while a stable boundary layer in rural areas during nighttime (Uno et al. 1992; Dupont et al. 1999).

The daytime contrast in surface resistance (r_s) is found to be positive almost everywhere (Fig. 6e), indicating that it is much harder for urban areas to produce evapotranspiration than rural areas. The nighttime Δr_s is much smaller than the daytime counterpart and can be quite uncertain due to the small latent heat flux at night (Fig. 6f). The urban–rural contrast in heat storage (ΔG) is positive during the daytime and negative during the nighttime (Figs. 6g,h). This is caused by the larger thermal admittance of surface materials in cities, which allows urban surfaces to store more heat during the day and thus release more heat at night (Oke et al. 2017; Grimmond and Oke 1999).

The extra factor that only appears in the attribution of urban–rural contrasts of 2-m air temperature and SWBGT is the 2-m layer aerodynamic resistance (r_a'). We find that $\Delta r_a'$, being negative, is weaker than Δr_a during the daytime (see Figs. 6i,c), implying that most of the resistance to convective heat transfer during the daytime lies between the surface and the 2-m level. This is because the size of turbulent eddies responsible for heat transfer scales with the distance from the surface (Katul et al. 2011; Li 2021). Between the surface and the 2-m level, the eddies are smaller and thus heat transfer is less efficient than their counterparts between the 2-m level and the atmosphere. During the night, the magnitude of $\Delta r_a'$
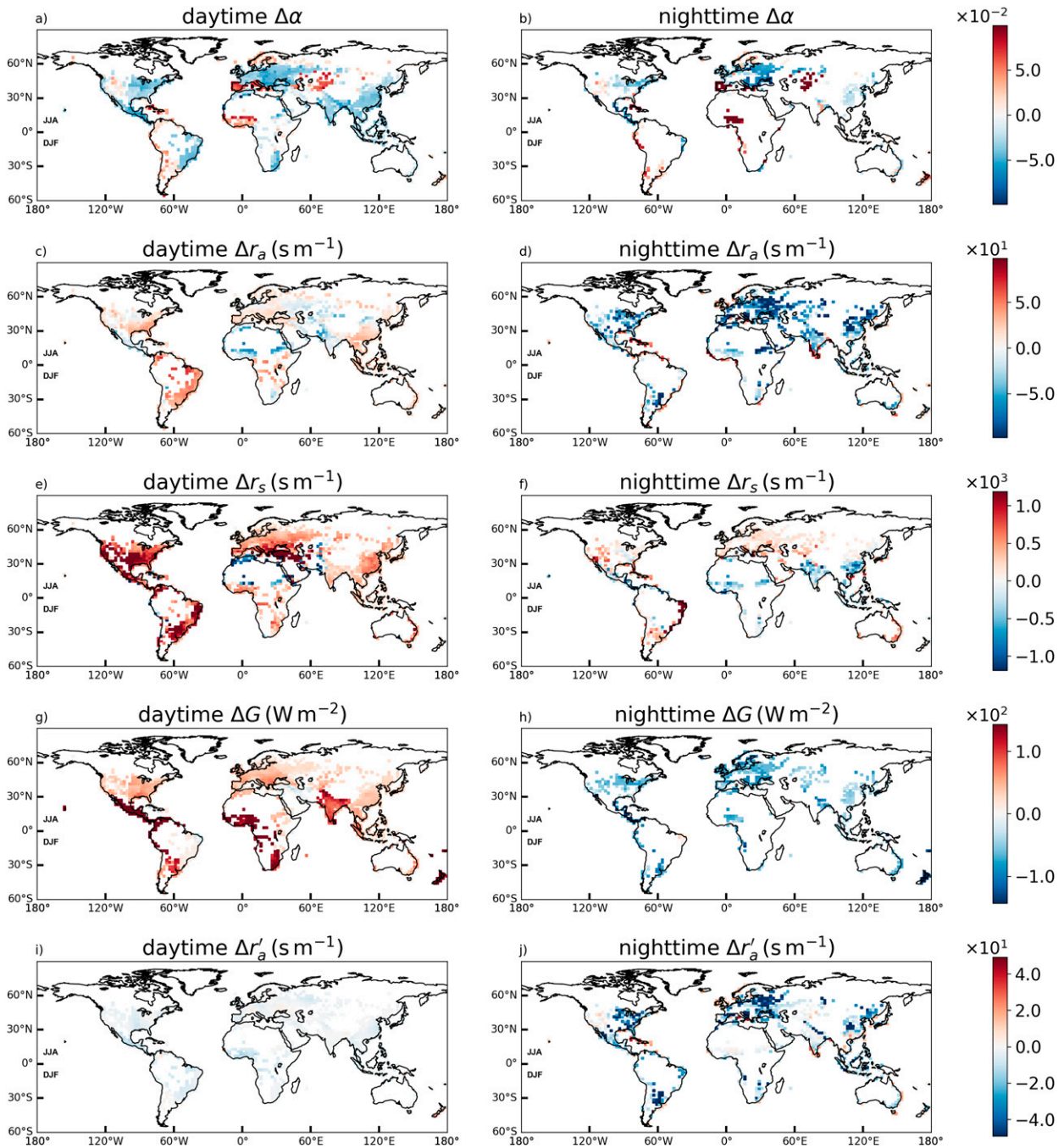
FIG. 6. The contrasts between urban and rural areas (Δ = urban − rural) in (a),(b) albedo (α), (c),(d) aerodynamic resistance (r_a), (e),(f) surface resistance (r_s), (g),(h) heat storage (G), and (i),(j) 2-m aerodynamic resistance (r_a') during (left) daytime and (right) nighttime. Note that the r_a' is only relevant for the attribution of 2-m air temperature and 2-m SWBGT in Fig. 3.

increases and $\Delta r_a'$ is similar to Δr_a (see Figs. 6j,d), suggesting that most of the resistance to convective heat transfer during the nighttime lies between the 2-m level and the atmosphere. In other words, the 2-m level becomes decoupled from the atmosphere due to the stable stratification, leading to stronger $\Delta r_a'$.

c. Contributions of biophysical factors

By multiplying the sensitivities (Fig. 4) and the urban–rural differences (Fig. 6), the contributions from these biophysical factors to the urban–rural contrast of canopy air SWBGT (ΔW_{ca}) are computed, as shown in Fig. 7. In the same way, we quantify the contributions to the urban–rural contrasts of 2-m
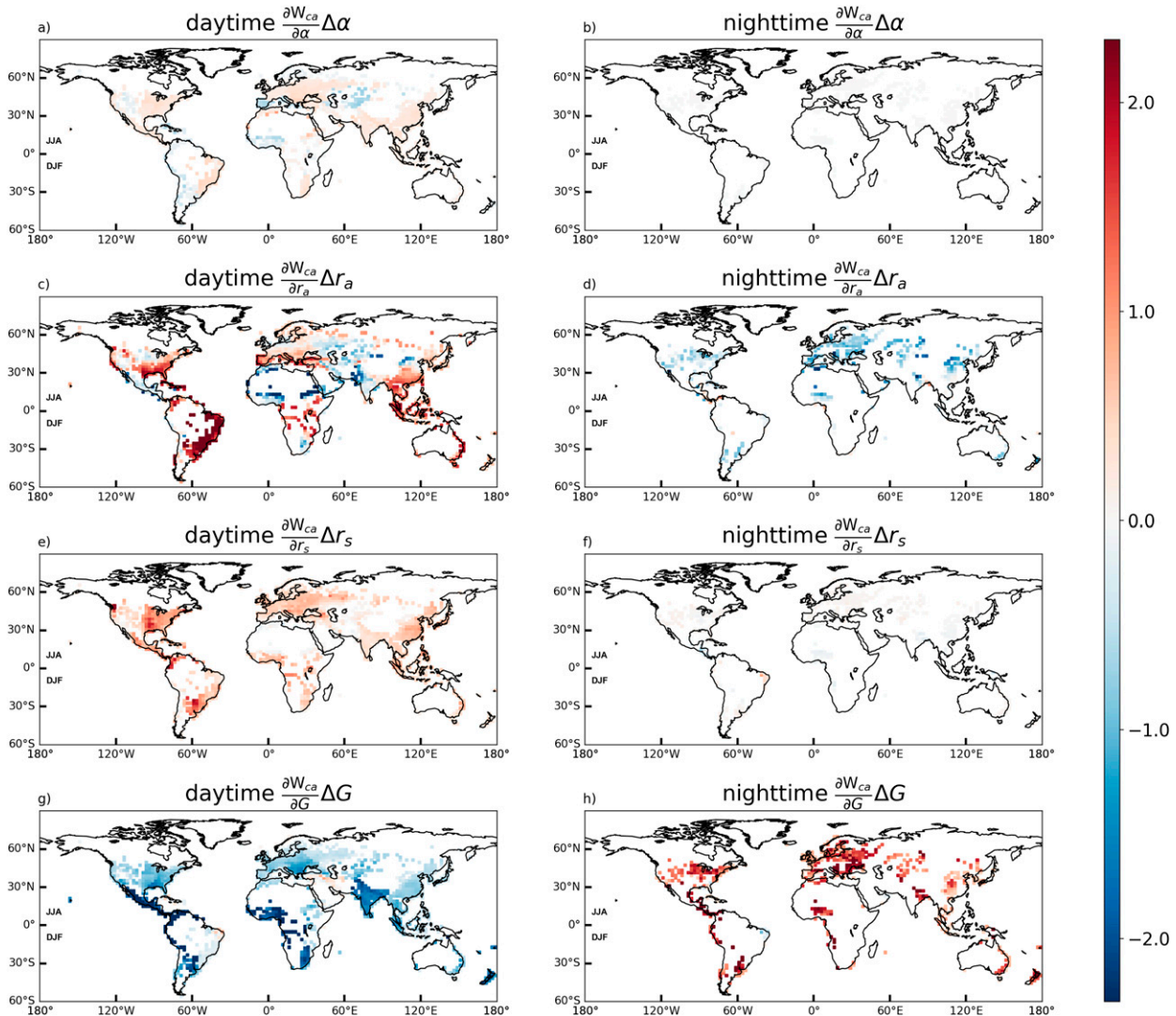
FIG. 7. The contributions to ΔW_{ca} from (a),(b) albedo $[(\partial W_{ca}/\partial\alpha)\Delta\alpha]$, (c),(d) aerodynamic resistance $[(\partial W_{ca}/\partial r_a)\Delta r_a]$, (e),(f) surface resistance $[(\partial W_{ca}/\partial r_s)\Delta r_s]$, and (g),(h) heat storage $[(\partial W_{ca}/\partial G)\Delta G]$ during (left) daytime and (right) nighttime.

SWBGT (W_2) (see Fig. 8), canopy air temperature (T_{ca}) (see Fig. S5), and 2-m air temperature (T_2) (see Figs. S4 and S6).

Before discussing the attribution results, we first use the numerical model simulated ΔW_{ca} (or ΔT_{ca}) to evaluate the TRM method by comparing the numerical model simulated results to the sum of the contributions from all biophysical components in the TRM method. It can be seen that the TRM attribution method is able to capture the numerical model simulation results with small root-mean-square errors (see Figs. S7 and S8). Nevertheless, at the 2-m level, the TRM-modeled ΔW_2 and ΔT_2 become more scattered compared to the simulated ones, which suggests that the extension of the TRM attribution method to the 2-m level introduces more uncertainties. This is not too surprising considering that the magnitudes of ΔW_2 and ΔT_2 are smaller than their canopy air counterparts.

Now we turn to the general patterns of the attribution results (Fig. 7). Here we use the same color bar for all the

factors in order to highlight their relative magnitude. During the daytime, albedo plays the least role in ΔW_{ca} among all biophysical factors (see Figs. 7a,b). That is because the model prescribes a very small urban–rural difference in albedo, which is on the order of 10^{-2} (see Figs. 6a,b). Other factors show stronger effects than albedo. Specifically, surface resistance contributes positively while heat storage contributes negatively during the daytime (see Figs. 7e,g), due to the combining effect of the large sensitivities (Fig. 4) and the large urban–rural differences in terms of these two factors (Fig. 6). Daytime effects of aerodynamic resistance show stronger spatial variability than other factors (Fig. 7c). At night, aerodynamic resistance and ground heat storage dominate the urban–rural difference in the canopy air SWBGT, with negative and positive contributions, respectively (Figs. 7d,h). Albedo and surface resistance have negligible effects at night (see Figs. 7b,f). The effect of ground storage shows a similar
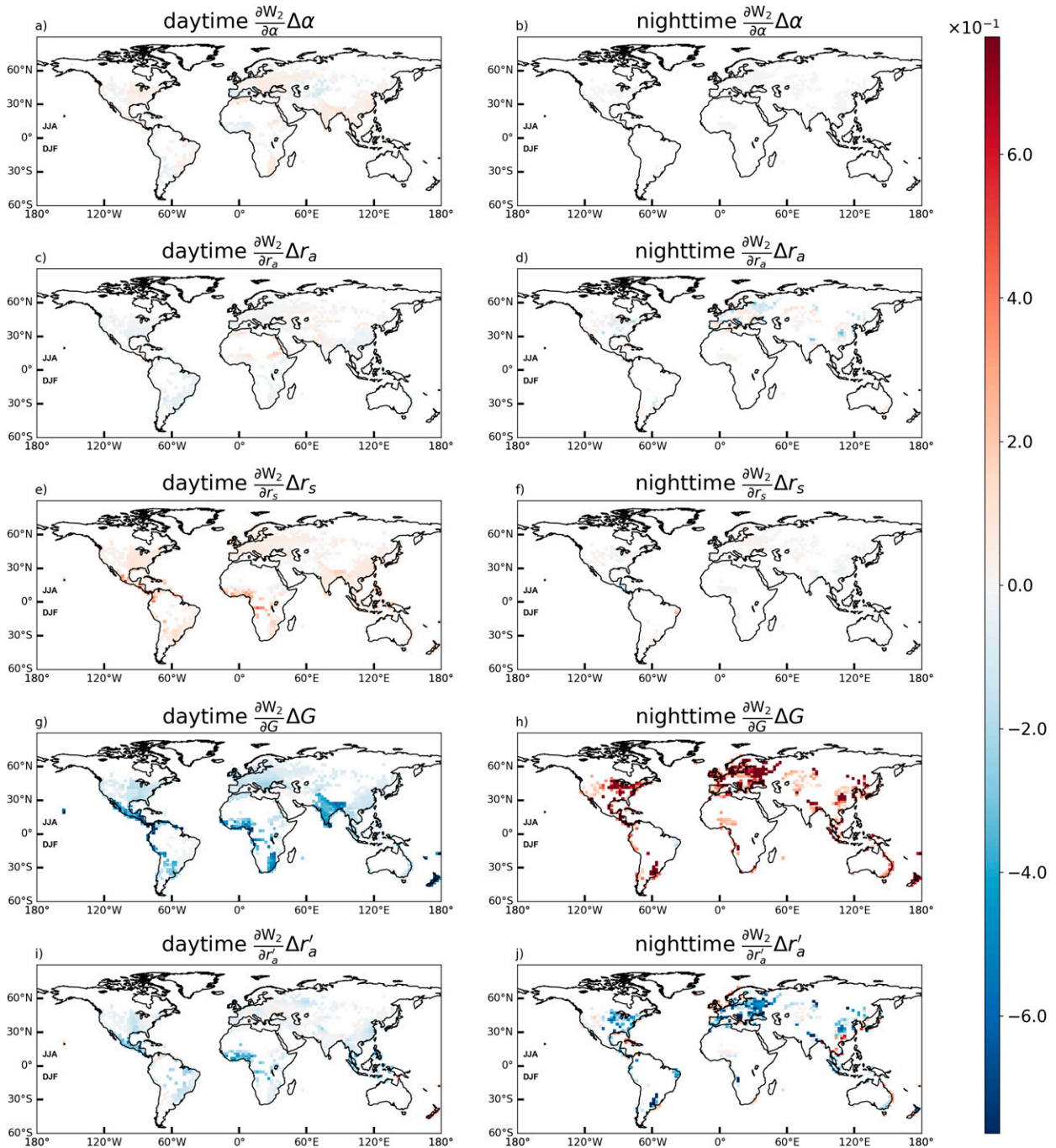
FIG. 8. The contributions to ΔW_2 from (a),(b) albedo $[(\partial W_2/\partial \alpha)\Delta \alpha]$, (c),(d) aerodynamic resistance $[(\partial W_2/\partial r_a)\Delta r_a]$, (e),(f) surface resistance $[(\partial W_2/\partial r_s)\Delta r_s]$, (g),(h) heat storage $[(\partial W_2/\partial G)\Delta G]$, and (i),(j) 2-m aerodynamic resistance $[(\partial W_2/\partial r_a')\Delta r_a']$ during (left) daytime and (right) nighttime.

magnitude between day and night, while others are weaker at night than during the day.

Furthermore, by comparing the results of ΔW_{ca} (Fig. 7) and ΔT_{ca} (Fig. S5), it is evident that the general patterns are similar but the effects of all four biophysical factors on ΔW_{ca} are reduced in terms of the magnitude due to the humidity

deficits in cities. In particular, surface resistance is the most dampened component such that the magnitude of the contribution of surface resistance to ΔW_{ca} is around 25% of that to ΔT_{ca}. Closer inspection reveals that the magnitude of the sensitivity of W_{ca} to r_s is about 25% of the sensitivity of T_{ca} to r_s. This result is again due to the fact that while the lack of
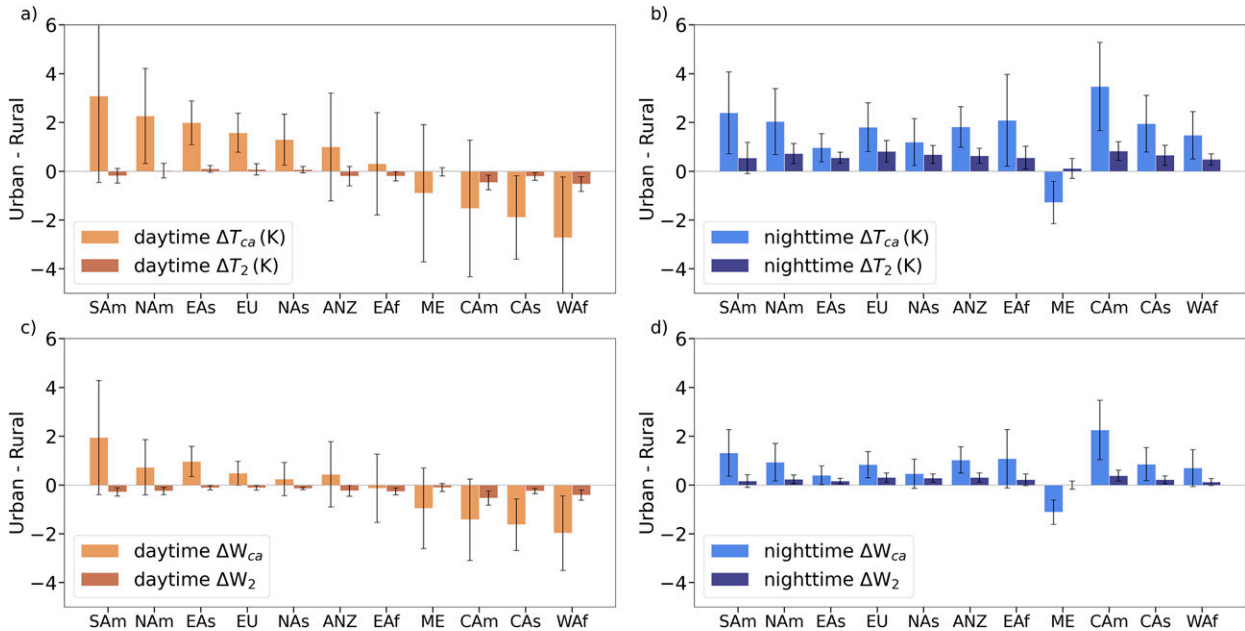
FIG. 9. Regional averages of urban–rural contrasts of (a),(b) canopy air temperature (ΔT_{ca}) and 2-m air temperature (ΔT_2), (c),(d) canopy air SWBGT (ΔW_{ca}) and 2-m SWBGT (ΔW_2) during (left) daytime and (right) nighttime. The error bars are the standard error and indicate the spatial variability.

evapotranspiration makes urban areas hotter, it also makes urban areas drier and hence slightly offsets the increase in ΔW_{ca} when compared to the increase in ΔT_{ca}.

At the 2-m level, results for albedo, surface resistance, and ground storage (see Fig. 8) exhibit much smaller magnitude than those at the canopy air level due to turbulent mixing. During the daytime, the main contributors are surface resistance (positive) and ground storage (negative), and there are no significant contributions of albedo and aerodynamic resistance. Nevertheless, it is worth noting that aerodynamic resistance makes the opposite contributions to ΔW_2 and ΔW_{ca} (cf. Fig. 8 and Fig. 7). This is because the sensitivity of W_2 to r_a has an opposite sign as the sensitivity of W_{ca} to r_a as discussed in section 3a. As for the 2-m aerodynamic resistance (r'_a) (see Figs. 8i,j), it consistently exerts negative effects because the majority of regions display negative urban–rural difference in r'_a (as in Figs. 6i,j). As a result, the negative contribution from ground storage (Fig. 8g) together with the negative contribution from the 2-m aerodynamic resistance causes a negative daytime ΔW_2 (see Fig. 3c). During the night, only ground storage (positive) and the 2-m aerodynamic resistance (negative) play a role in ΔW_2 (see Figs. 8h,j).

d. Regionally averaged attributions of ΔT_{ca}, ΔT_2, ΔW_{ca}, and ΔW_2

Because the urban–rural differences in temperature and SWBGT display an evident dependence on geographic locations (see Figs. 2 and 3), in this section results are analyzed in the manner of regional averages. Region boundaries are defined in a similar way as McCarthy et al. (2010) (see Fig. 2a with the region abbreviations defined in the caption). Figure 9

shows the regional averages of ΔT_{ca}, ΔT_2, ΔW_{ca}, and ΔW_2 during the daytime and nighttime. Comparing the upper panels against the lower ones, the similarity between the averaged urban–rural contrasts of temperature and SWBGT shows up clearly over all regions. The regional averages of daytime ΔT_{ca} and ΔW_{ca} are positive except in the Middle East, Central America, Central Asia, and West Africa. During the nighttime, all regions but the Middle East show positive values of ΔT_{ca} and ΔW_{ca}. In terms of the 2-m air temperature and SWBGT, the regional averages of ΔT_2 and ΔW_2 mostly vanish during the day except for Central America and West Africa while exhibiting weakly positive signals at night. Note that the error bars are very large especially for regions with negative ΔT_2 and ΔW_2, indicating significant spatial variability within each region. After case-by-case investigations of all 11 regions, we select North America, Central America, South America, and the Middle East to highlight four distinctive regional patterns of the urban–rural differences in heat stress and their attributions (Fig. 10). The results for the urban–rural differences in temperature are presented in Fig. S9.

Starting off from the canopy air level, in North America, surface resistance (r_s) is the leading cause of the positive ΔT_{ca} during the daytime (Fig. S9a), indicating the dominant role of evapotranspiration in controlling the urban–rural differences in canopy air temperature in this region. Such results are consistent with the finding of previous studies that the relationship between surface UHI and background climate is largely explained by evapotranspiration (Li et al. 2019; Manoli et al. 2019). For daytime W_{ca} (Fig. 10a), the contribution of surface resistance remains strong but aerodynamic resistance plays an equally important role. Heat storage (G) has a strong
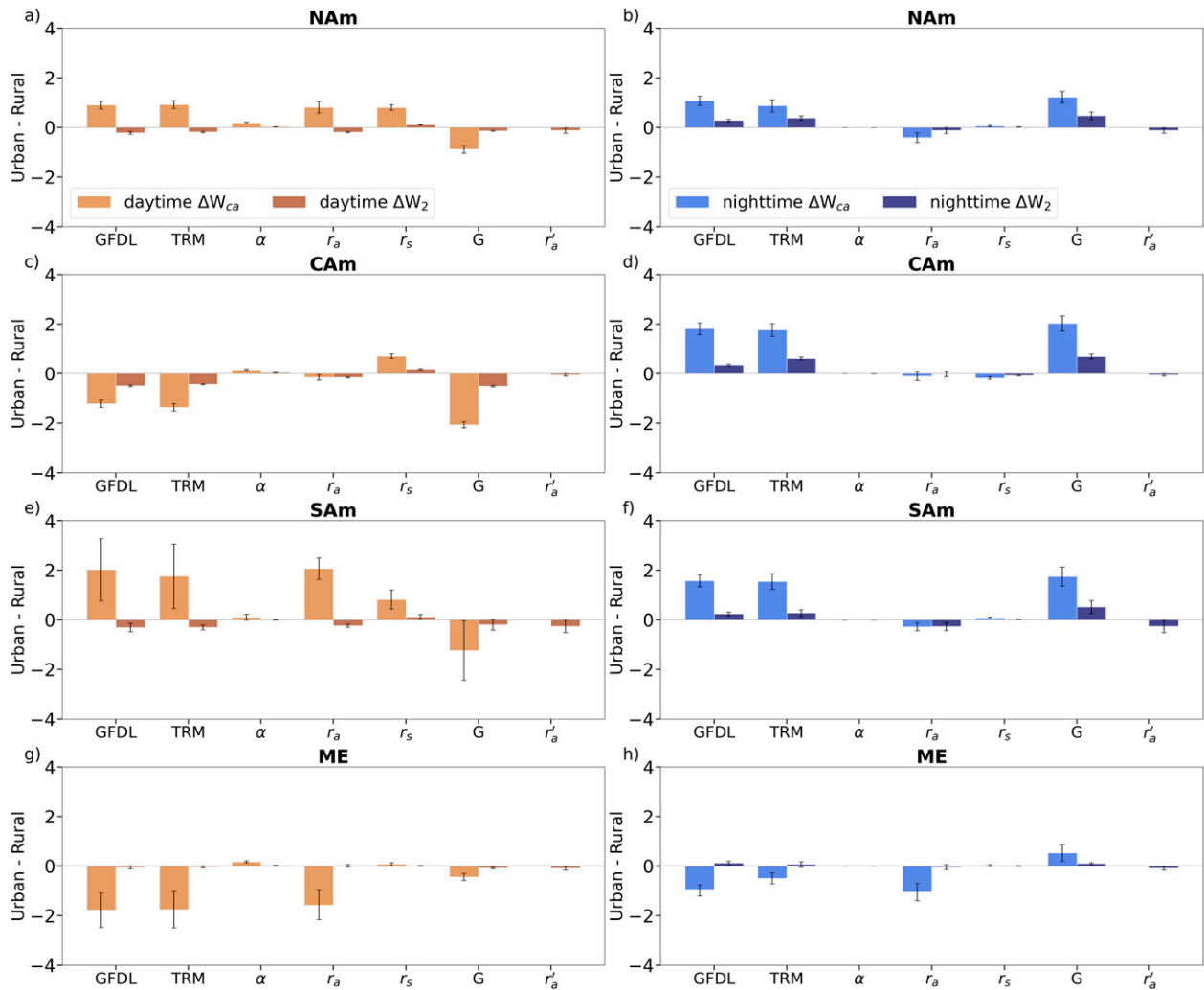
FIG. 10. Regionally averaged attribution results for urban–rural contrasts of canopy air SWBGT (ΔW_{ca}) and 2-m SWBGT (ΔW_2) over (a),(b) North America (NAm), (c),(d) Central America (CAm), (e),(f) South America (SAm), and (g),(h) Middle East (ME) during (left) daytime and (right) nighttime. ΔW_{ca} and ΔW_2 are represented by yellow and brown bars over daytime and by blue and dark blue bars over nighttime. GFDL represents the simulated ΔW_{ca} and ΔW_2 by the numerical model. TRM represents the sum of the four contributions calculated from the TRM method. The terms α, r_a, r_s, G, and r_a' represent the contributions from albedo, aerodynamic resistance between the surface and the atmosphere, surface resistance, heat storage, and aerodynamic resistance between the 2-m level and the atmosphere, respectively. The error bars are the standard error and indicate the spatial variability.

negative effect (Fig. S9a and Fig. 10a). When the negative contribution of heat storage exceeds the positive contribution of surface resistance, daytime urban–rural contrasts of T_{ca} and W_{ca} become negative, as in the case of Central America (Fig. S9c and Fig. 10c) and other regions with negative temperature/SWBGT differences (not shown). Close inspection reveals that the numerical model prescribes very large thermal admittance for urban roofs in these regions (Jackson et al. 2010; Oleson et al. 2011; Oleson and Feddema 2020; Wang et al. 2020a). Since the capability of a surface to store heat is largely governed by thermal admittance, this explains why these regions have very strong negative contributions from heat storage during the daytime. Previous studies also showed that the urban heat sink could occur during the

daytime when urban surfaces have greater heat absorption and when rural areas have dry, bare soil with low thermal inertia and low evaporative cooling (Carnahan and Larson 1990).

In South America (Fig. S9e and Fig. 10e), the positive effect from aerodynamic resistance (r_a) to ΔT_{ca} and ΔW_{ca} becomes very large and even exceeds that from surface resistance in terms of ΔW_{ca} during the daytime, which leads to positive ΔT_{ca} and ΔW_{ca}. In contrast, aerodynamic resistance (r_a) makes a large negative contribution in the Middle East (Fig. S9g and Fig. 10g), causing ΔT_{ca} and ΔW_{ca} to be negative. These results are broadly consistent with recent work on the spatial variability of daytime surface UHI (Zhao et al. 2014; Li et al. 2019; Manoli et al. 2019). Cities in humid climates (South America) are often surrounded by forests, which

might convect heat more efficiently than buildings. Hence aerodynamic resistance makes a positive contribution to daytime ΔT_{ca} and ΔW_{ca}. On the other hand, in dry regions (Middle East) rural areas are characterized by short vegetation and deserts, and cities can have a higher convection efficiency, as discussed in section 3b. As a result, the contribution from aerodynamic resistance becomes strongly negative and the positive contribution from surface resistance is weak in these dry regions, which therefore causes negative daytime ΔT_{ca} and ΔW_{ca}.

During the night, the attribution results are more consistent across different regions (e.g., North America, Central America, and South America), characterized by a dominant positive contribution from the ground heat storage and thus positive ΔT_{ca} and ΔW_{ca} (see Figs. S9b,d,f and Figs. 10b,d,f). However, in the Middle East, the negative effect of aerodynamic resistance exceeds the positive effect of heat storage release, resulting in negative ΔT_{ca} and ΔW_{ca}.

Concerning the 2-m level results, the urban–rural contrast of all variables becomes nearly zero during the day regardless of regions as a result of strong mixing (Figs. S9a,c,e,g and Figs. 10a,c,e,g). Similar to what was found in Venter et al. (2021) and Stewart et al. (2021), the magnitude of the simulated ΔT_{ca} (which is closer to the surface UHI in the observations) far exceeds that of ΔT_2 (which is closer to the near-surface UHI in the observations). At night, the primary heat source of the near atmosphere comes from heat storage accumulated in the daytime (Oke et al. 2017; Grimmond and Oke 1999). As a result, these four regions have slightly positive ΔT_2 and ΔW_2 during the night, with a magnitude much less than their canopy air counterparts.

4. Conclusions

In this study, we develop a methodology to quantify the physical processes contributing to the urban–rural difference in heat stress based on the two-resistance mechanism (TRM) method. The improved TRM method is applied to diagnosing urban–rural contrast of canopy air temperature/SWBGT simulated by the GFDL LM4.0 coupled with a UCM. Results indicate that contributions of the four biophysical factors (albedo, aerodynamic resistance, surface resistance, and ground heat flux or heat storage) to the urban–rural differences in canopy air SWBGT (ΔW_{ca}) vary diurnally and geographically. The urban–rural contrasts of canopy air SWBGT (ΔW_{ca}) and canopy air temperature (ΔT_{ca}) share similarity, but the magnitude of ΔW_{ca} is smaller due to moisture deficits in cities.

We further apply the attribution framework to study four regions (North America, Central America, South America, and the Middle East). In North America, surface resistance makes a stronger contribution than ground heat flux during the daytime, while it is the opposite in Central America. Aerodynamic resistance can make positive (e.g., North America and South America), negligible (e.g., Central America), or negative (e.g., Middle East) contributions during the daytime. The nighttime results are more consistent across geographic regions with mostly positive urban–rural differences in temperatures and

heat stresses due to the strongly positive contributions from heat storage. Only in the Middle East does the negative contribution of aerodynamic resistance overweight the positive contribution from ground heat flux at night.

We also extend the method to studying the 2-m air temperature/SWBGT. A new biophysical factor, the 2-m level aerodynamic resistance (r_a'), is introduced in the attribution framework. Overall, ΔW_2 and ΔT_2 share similar patterns as ΔW_{ca} and ΔT_{ca}, respectively, but with much smaller magnitude due to turbulent mixing in the surface layer.

5. Discussion

This study has several implications that are important to appreciate. First, the methodology to quantitatively attribute urban–rural differences in heat stress is generic and can be applied to any heat stress index that is a function of temperature and humidity. Therefore, it allows for the intercomparison of different heat stress indices as well as the intercomparison of different numerical models. However, we caution that this method is not applicable to heat indices that are also functions of radiation and wind speed. Further development of attribution methods for more complicated heat stress indices is still needed.

Second, the traditional definition of 2-m air temperature and heat stress does not necessarily facilitate a clean comparison between urban and rural thermal conditions. Since urban areas often have a much larger displacement height, the so-called "2-m" air temperature (and heat stress) correspond to a higher physical height in urban areas than in rural areas. This might partly explain why the model yields negative daytime urban–rural differences in heat stress. Some models try to correct such effects in an ad hoc way, but it remains unclear what constitutes a clean comparison in numerical models that do not resolve the temperature/humidity profiles within the urban canopy.

Third, the attribution method used in this study highlights two well-known causes of the positive urban–rural differences in temperatures and heat stresses: the lack of evapotranspiration (a daytime effect) and the stronger release of heat storage (a nighttime effect). However, the daytime urban–rural contrasts of canopy air temperature and heat stress are found to be negative in places where urban areas are surrounded by short vegetation (e.g., arid regions) so that urban areas have lower aerodynamic resistances and in places where urban materials have very large thermal admittance. These factors have been less studied but are physically possible. They highlight that it is critical for numerical models to prescribe the correct roughness lengths and thermal properties to capture the urban–rural contrasts of temperature and heat stress.

Fourth, while the attribution method can shed many insights, applying it to diagnosing numerical model outputs should proceed with caution. The attribution method is developed for a bulk surface. However, numerical models often treat urban (and rural) areas as having multiple heat sources and sinks. As a result, it is not straightforward to construct a bulk surface temperature using numerical model outputs. Extending the TRM attribution method to the 2-m level is more

challenging. As the magnitude of simulated urban–rural differences in temperature and heat stress at the 2-m level is smaller, the TRM modeled urban–rural differences in temperature and heat stress at the 2-m level are more scattered. Moreover, some parameters needed by the attribution method and inferred from numerical model outputs (e.g., aerodynamic resistance) might become physically meaningless (e.g., aerodynamic resistance is negative). The current practice is to simply discard such data. Further developments of attribution methods are needed to verify the consequence of such a practice.

Last but not least, it is worth noting that the attribution method, as a diagnostic method, does not provide any information regarding the validity of the numerical model results against real-world observations. Validation against observations is outside the scope of this study but is critical for establishing confidence in the numerical model results.

Data availability statement. All data used in this analysis are publicly available at https://doi.org/10.5281/zenodo.6629390, or by request to the corresponding author.

REFERENCES

Anderson, G. B., M. L. Bell, and R. D. Peng, 2013: Methods to calculate the heat index as an exposure metric in environmental health research. *Environ. Health Perspect.*, **121**, 1111–1119, https://doi.org/10.1289/ehp.1206273.

Barriopedro, D., E. M. Fischer, J. Luterbacher, R. M. Trigo, and R. García-Herrera, 2011: The hot summer of 2010: Redrawing the temperature record map of Europe. *Science*, **332**, 220–224, https://doi.org/10.1126/science.1201224.

Best, M., and C. Grimmond, 2015: Key conclusions of the First International Urban Land Surface Model Comparison Project. *Bull. Amer. Meteor. Soc.*, **96**, 805–819, https://doi.org/10.1175/BAMS-D-14-00122.1.

Bonan, G., 2019: *Climate Change and Terrestrial Ecosystem Modeling*. Cambridge University Press, 437 pp.

Buzan, J. R., K. Oleson, and M. Huber, 2015: Implementation and comparison of a suite of heat stress metrics within the Community Land Model version 4.5. *Geosci. Model Dev.*, **8**, 151–170, https://doi.org/10.5194/gmd-8-151-2015.

Carnahan, W. H., and R. C. Larson, 1990: An analysis of an urban heat sink. *Remote Sens. Environ.*, **33**, 65–71, https://doi.org/10.1016/0034-4257(90)90056-R.

Chakraborty, T., Z. S. Venter, Y. Qian, and X. Lee, 2022: Lower urban humidity moderates outdoor heat stress. *AGU Adv.*, **3**, e2022AV000729, https://doi.org/10.1029/2022AV000729.

Chen, C., L. Wang, R. B. Myneni, and D. Li, 2020: Attribution of land-use/land-cover change induced surface temperature anomaly: How accurate is the first-order Taylor series expansion? *J. Geophys. Res. Biogeosci.*, **125**, e2020JG005787, https://doi.org/10.1029/2020JG005787.

Chen, L., and P. A. Dirmeyer, 2016: Adapting observationally based metrics of biogeophysical feedbacks from land cover/land use change to climate modeling. *Environ. Res. Lett.*, **1**, 34 002–34 015, https://doi.org/10.1088/1748-9326/11/3/034002.

Dunne, J. P., R. J. Stouffer, and J. G. John, 2013: Reductions in labour capacity from heat stress under climate warming. *Nat. Climate Change*, **3**, 563–566, https://doi.org/10.1038/nclimate1827.

Dupont, E., L. Menut, B. Carissimo, J. Pelon, and P. Flamant, 1999: Comparison between the atmospheric boundary layer in Paris and its rural suburbs during the ECLAP experiment. *Atmos. Environ.*, **33**, 979–994, https://doi.org/10.1016/S1352-2310(98)00216-7.

Fanger, P. O., 1972: *Thermal Comfort: Analysis and Applications in Environmental Engineering*. McGraw-Hill, 244 pp.

Fischer, E. M., K. W. Oleson, and D. M. Lawrence, 2012: Contrasting urban and rural heat stress responses to climate change. *Geophys. Res. Lett.*, **39**, L03705, https://doi.org/10.1029/2011GL050576.

Garratt, J., 1994: *The Atmospheric Boundary Layer*. Cambridge Atmospheric and Space Science Series, Cambridge University Press, 316 pp.

Grimmond, C. S. B., and T. R. Oke, 1999: Heat storage in urban areas: Local-scale observations and evaluation of a simple model. *J. Appl. Meteor. Climatol.*, **38**, 922–940, https://doi.org/10.1175/1520-0450(1999)038<0922:HSIUAL>2.0.CO;2.

——, and Coauthors, 2010: The international urban energy balance models comparison project: First results from Phase 1. *J. Appl. Meteor. Climatol.*, **49**, 1268–1292, https://doi.org/10.1175/2010JAMC2354.1.

——, and Coauthors, 2011: Initial results from phase 2 of the international urban energy balance model comparison. *Int. J. Climatol.*, **31**, 244–272, https://doi.org/10.1002/joc.2227.

Grimmond, S., 2007: Urbanization and global environmental change: Local effects of urban warming. *Geogr. J.*, **173**, 83–88, https://doi.org/10.1111/j.1475-4959.2007.232_3.x.

Grundstein, A., and E. Cooper, 2018: Assessment of the Australian Bureau of Meteorology wet bulb globe temperature model using weather station data. *Int. J. Biometeor.*, **62**, 2205–2213, https://doi.org/10.1007/s00484-018-1624-1.

Howard, L., 1833: *The Climate of London: Deduced from Meteorological Observations Made in the Metropolis and at Various Places around It*. Vol. 3, Harvey and Darton, J. and A. Arch, Longman, Hatchard, S. Highley, and R. Hunter, 383 pp.

Jackson, P. S., 1981: On the displacement height in the logarithmic velocity profile. *J. Fluid Mech.*, **111**, 15–25, https://doi.org/10.1017/S0022112081002279.

Jackson, T. L., J. J. Feddema, K. W. Oleson, G. B. Bonan, and J. T. Bauer, 2010: Parameterization of urban characteristics for global climate modeling. *Ann. Assoc. Amer. Geogr.*, **100**, 848–865, https://doi.org/10.1080/00045608.2010.497328.

Katul, G. G., A. G. Konings, and A. Porporato, 2011: Mean velocity profile in a sheared and thermally stratified atmospheric boundary layer. *Phys. Rev. Lett.*, **107**, 268502, https://doi.org/10.1103/PhysRevLett.107.268502.

Kong, Q., and M. Huber, 2022: Explicit calculations of wet-bulb globe temperature compared with approximations and why it matters for labor productivity. *Earth's Future*, **10**, e2021EF002334, https://doi.org/10.1029/2021EF002334.

Kusaka, H., H. Kondo, Y. Kikegawa, and F. Kimura, 2001: A simple single-layer urban canopy model for atmospheric models: Comparison with multi-layer and slab models. *Bound.-Layer Meteor.*, **101**, 329–358, https://doi.org/10.1023/A:1019207923078.

Landsberg, H. E., 1981: *The Urban Climate*. International Geophysics Series, Vol. 28. Academic Press, 275 pp.

Li, D., 2021: The O'KEYPS equation and 60 years beyond. *Bound.-Layer Meteor.*, **179**, 19–42, https://doi.org/10.1007/s10546-020-00585-y.

——, and E. Bou-Zeid, 2014: Quality and sensitivity of high-resolution numerical simulation of urban heat islands. *Environ. Res. Lett.*, **9**, 055001, https://doi.org/10.1088/1748-9326/9/5/055001.

——, S. Malyshev, and E. Shevliakova, 2016a: Exploring historical and future urban climate in the earth system modeling framework: 1. Model development and evaluation. *J. Adv. Model. Earth Syst.*, **8**, 917–935, https://doi.org/10.1002/2015MS000578.

——, ——, and ——, 2016b: Exploring historical and future urban climate in the Earth system modeling framework: 2. Impact of urban land use over the continental United States. *J. Adv. Model. Earth Syst.*, **8**, 936–953, https://doi.org/10.1002/2015MS000579.

——, W. Liao, A. J. Rigden, X. Liu, D. Wang, S. Malyshev, and E. Shevliakova, 2019: Urban heat island: Aerodynamics or imperviousness? *Sci. Adv.*, **5**, eaau4299, https://doi.org/10.1126/sciadv.aau4299.

Liao, W., A. J. Rigden, and D. Li, 2018: Attribution of local temperature response to deforestation. *J. Geophys. Res. Biogeosci.*, **123**, 1572–1587, https://doi.org/10.1029/2018JG004401.

——, X. Liu, E. Burakowski, D. Wang, L. Wang, and D. Li, 2020: Sensitivities and responses of land surface temperature to deforestation-induced biophysical changes in two global Earth system models. *J. Climate*, **33**, 8381–8399, https://doi.org/10.1175/JCLI-D-19-0725.1.

——, D. Li, S. Malyshev, E. Shevliakova, H. Zhang, and X. Liu, 2021: Amplified increases of compound hot extremes over urban land in China. *Geophys. Res. Lett.*, **48**, e2020GL091252, https://doi.org/10.1029/2020GL091252.

Manoli, G., and Coauthors, 2019: Magnitude of urban heat islands largely explained by climate and population. *Nature*, **573**, 55–60, https://doi.org/10.1038/s41586-019-1512-9.

Masson, V., 2000: A physically-based scheme for the urban energy budget in atmospheric models. *Bound.-Layer Meteor.*, **94**, 357–397, https://doi.org/10.1023/A:1002463829265.

Matthies, F., G. Bickler, S. Hales, and N. C. Marín, 2008: *Heat-Health Action Plans Guidance*. World Health Organization, 45 pp.

McCarthy, M. P., M. J. Best, and R. A. Betts, 2010: Climate change in cities due to global warming and urban effects. *Geophys. Res. Lett.*, **37**, L09705, https://doi.org/10.1029/2010GL042845.

Meili, N., and Coauthors, 2020: An urban ecohydrological model to quantify the effect of vegetation on urban climate and hydrology (UT&C v1. 0). *Geosci. Model Dev.*, **13**, 335–362, https://doi.org/10.5194/gmd-13-335-2020.

Middel, A., S. AlKhaled, F. A. Schneider, B. Hagen, and P. Coseo, 2021: 50 grades of shade. *Bull. Amer. Meteor. Soc.*, **102**, E1805–E1820, https://doi.org/10.1175/BAMS-D-20-0193.1.

Monteith, J. L., and M. H. Unsworth, 2008: *Principles of Environmental Physics*. 3rd ed. Elsevier, 418 pp.

Moon, M., D. Li, W. Liao, A. J. Rigden, and M. A. Friedl, 2020: Modification of surface energy balance during springtime: The relative importance of biophysical and meteorological changes. *Agric. For. Meteor.*, **284**, 107905, https://doi.org/10.1016/j.agrformet.2020.107905.

National Weather Service, 2021: Summary of natural hazard statistics for 2020 in the United States. Accessed 7 June 2022, https://www.weather.gov/media/hazstat/sum20.pdf.

Oke, T. R., 1978: *Boundary Layer Climates*. Wiley, 372 pp.

——, 1981: Canyon geometry and the nocturnal urban heat island: Comparison of scale model and field observations. *J. Climatol.*, **1**, 237–254, https://doi.org/10.1002/joc.3370010304.

——, 1982: The energetic basis of the urban heat island. *Quart. J. Roy. Meteor. Soc.*, **108** (455), 1–24, https://doi.org/10.1002/qj.49710845502.

——, G. Mills, A. Christen, and J. A. Voogt, 2017: *Urban Climates*. Cambridge University Press, 548 pp.

Oleson, K., 2012: Contrasts between urban and rural climate in CCSM4 CMIP5 climate change scenarios. *J. Climate*, **25**, 1390–1412, https://doi.org/10.1175/JCLI-D-11-00098.1.

——, and Coauthors, 2013: Technical description of version 4.5 of the Community Land Model (CLM). NCAR Tech. Note NCAR/TN-503+STR, 420 pp., https://doi.org/10.5065/D6RR1W7M.

Oleson, K. W., and J. Feddema, 2020: Parameterization and surface data improvements and new capabilities for the Community Land Model Urban (CLMU). *J. Adv. Model. Earth Syst.*, **12**, e2018MS001586, https://doi.org/10.1029/2018MS001586.

——, G. B. Bonan, J. Feddema, and M. Vertenstein, 2008a: An urban parameterization for a global climate model. Part II: Sensitivity to input parameters and the simulated urban heat island in offline simulations. *J. Appl. Meteor. Climatol.*, **47**, 1061–1076, https://doi.org/10.1175/2007JAMC1598.1.

——, ——, ——, ——, and C. S. B. Grimmond, 2008b: An urban parameterization for a global climate model. Part I: Formulation and evaluation for two cities. *J. Appl. Meteor. Climatol.*, **47**, 1038–1060, https://doi.org/10.1175/2007JAMC1597.1.

——, ——, ——, and T. Jackson, 2011: An examination of urban heat island characteristics in a global climate model. *Int. J. Climatol.*, **31**, 1848–1865, https://doi.org/10.1002/joc.2201.

——, A. Monaghan, O. Wilhelmi, M. Barlage, N. Brunsell, J. Feddema, L. Hu, and D. F. Steinhoff, 2015: Interactions between urbanization, heat stress, and climate change. *Climatic Change*, **129**, 525–541, https://doi.org/10.1007/s10584-013-0936-8.

Rigden, A. J., and D. Li, 2017: Attribution of surface temperature anomalies induced by land use and land cover changes. *Geophys. Res. Lett.*, **44**, 6814–6822, https://doi.org/10.1002/2017GL073811.

Robine, J.-M., S. L. K. Cheung, S. Le Roy, H. Van Oyen, C. Griffiths, J.-P. Michel, and F. R. Herrmann, 2008: Death toll exceeded 70,000 in Europe during the summer of 2003. *C. R. Biol.*, **331**, 171–178, https://doi.org/10.1016/j.crvi.2007.12.001.

Seto, K. C., and J. M. Shepherd, 2009: Global urban land-use trends and climate impacts. *Curr. Opin. Environ. Sustainability*, **1**, 89–95, https://doi.org/10.1016/j.cosust.2009.07.012.

Sheffield, J., G. Goteti, and E. F. Wood, 2006: Development of a 50-year high-resolution global dataset of meteorological forcings for land surface modeling. *J. Climate*, **19**, 3088–3111, https://doi.org/10.1175/JCLI3790.1.

Sherwood, S. C., and M. Huber, 2010: An adaptability limit to climate change due to heat stress. *Proc. Natl. Acad. Sci. USA*, **107**, 9552–9555, https://doi.org/10.1073/pnas.0913352107.

Stewart, I., E. Krayenhoff, J. Voogt, J. Lachapelle, M. Allen, and A. Broadbent, 2021: Time evolution of the surface urban heat island. *Earth's Future*, **9**, e2021EF002178, https://doi.org/10.1029/2021EF002178.

Stull, R. B., 1988: *An Introduction to Boundary Layer Meteorology*. Springer, 670 pp.

Uno, I., S. Wakamatsu, H. Ueda, and A. Nakamura, 1992: Observed structure of the nocturnal urban boundary layer and

its evolution into a convective mixed layer. *Atmos. Environ.*, **26B**, 45–57, https://doi.org/10.1016/0957-1272(92)90036-R.

Venter, Z. S., T. Chakraborty, and X. Lee, 2021: Crowdsourced air temperatures contrast satellite measures of the urban heat island and its mechanisms. *Sci. Adv.*, **7**, eabb9569, https://doi.org/10.1126/sciadv.abb9569.

Wang, L., and D. Li, 2021: Urban heat islands during heat waves: A comparative study between Boston and Phoenix. *J. Appl. Meteor. Climatol.*, **60**, 621–641, https://doi.org/10.1175/JAMC-D-20-0132.1.

——, M. Huang, and D. Li, 2020a: Where are white roofs more effective in cooling the surface? *Geophys. Res. Lett.*, **47**, e2020GL087853, https://doi.org/10.1029/2020GL087853.

——, D. Li, N. Zhang, J. Sun, and W. Guo, 2020b: Surface urban heat and cool islands and their drivers: An observational study in Nanjing, China. *J. Appl. Meteor. Climatol.*, **59**, 1987–2000, https://doi.org/10.1175/JAMC-D-20-0089.1.

Wang, P., D. Li, W. Liao, A. Rigden, and W. Wang, 2019: Contrasting evaporative responses of ecosystems to heatwaves traced to the opposing roles of vapor pressure deficit and surface resistance. *Water Resour. Res.*, **55**, 4550–4563, https://doi.org/10.1029/2019WR024771.

Willett, K. M., and S. Sherwood, 2012: Exceedance of heat index thresholds for 15 regions under a warming climate using the wet-bulb globe temperature. *Int. J. Climatol.*, **32**, 161–177, https://doi.org/10.1002/joc.2257.

World Meterological Organization, 2021: June ends with exceptional heat. Accessed 8 October 2021, https://public.wmo.int/en/media/news/june-ends-exceptional-heat.

Yow, D. M., 2007: Urban heat islands: Observations, impacts, and adaptation. *Geogr. Compass*, **1**, 1227–1251, https://doi.org/10.1111/j.1749-8198.2007.00063.x.

Zhang, Y., I. Held, and S. Fueglistaler, 2021: Projections of tropical heat stress constrained by atmospheric dynamics. *Nat. Geosci.*, **14**, 133–137, https://doi.org/10.1038/s41561-021-00695-3.

Zhao, L., X. Lee, R. B. Smith, and K. Oleson, 2014: Strong contributions of local background climate to urban heat islands. *Nature*, **511**, 216–219, https://doi.org/10.1038/nature13462.